catalysts

MDPI

Article

Ni/NiO Nanocomposites with Rich Oxygen Vacancies as High-Performance Catalysts for Nitrophenol Hydrogenation

Jun Zhou [1], Yue Zhang [1], Song Li [1,*] and Jing Chen [2,*]

[1] Key Lab for Anisotropy and Texture of Materials (MoE), School of Materials Science and Engineering, Northeastern University, Shenyang 110819, China; hafouniu@163.com (J.Z.); zhangyue@stumail.neu.edu.cn (Y.Z.)

[2] Institute of Microscale Optoelectronics (IMO), Shenzhen University, Shenzhen 518060, China

* Correspondence: lis@atm.neu.edu.cn (S.L.); jingchen@szu.edu.cn (J.C.)

Received: 20 October 2019; Accepted: 9 November 2019; Published: 11 November 2019

Abstract: Heterogeneous catalysis often involves charge transfer between adsorbed molecules and the surface of catalyst, and thus their activity depends on the surface charge density. The efficiency of charge transfer could be optimized by adjusting the concentration of oxygen vacancies (O_v). In this work, hexagonal $Ni(OH)_2$ nanoparticles were initially synthesized by a hydrothermal process using aluminum powder as the sacrificial agent, and were then converted into 2D Ni/NiO nanocomposites through in situ reduction in hydrogen flow. The oxygen vacancy concentration in the NiO nanosheet could be well-controlled by adjusting the reduction temperature. This resulted in strikingly high activities for hydrogenation of nitrophenol. The Ni/NiO nanocomposite could easily be recovered by a magnetic field for reuse. The present finding is beneficial for producing better hydrogenation catalysts and paves the way for the design of highly efficient catalysts.

Keywords: metal-oxide interaction; oxygen vacancy; hydrogenation; catalyst

1. Introduction

Hydrogenation is an important class of industrial reactions for converting unsaturated hydrocarbons or nitroarenes to produce fine chemicals [1–5]. Estimations show that a quarter of all chemical processes include at least one catalytic hydrogenation step [6]. Hydrogenation of nitrophenol (NP) to aminophenol is a typical reaction important for both environmental remediation and chemical stock production, considering that nitrophenols are hard-to-degrade compounds and exist widely in industrial wastewater [7]. The aminophenols are important intermediate products for synthesizing fine chemicals [8–10]. Supported nanoparticles of noble metals, including Pd, Au, and their alloys, exhibit high activity for hydrogenation of nitrophenols [11–15]. Though conversion efficiency is high, intensive costs of noble metals limit their large-scale industrial employment. To reduce the cost and energy-consumption of the processing, highly active catalysts comprising non-precious metals are highly preferable. Many efforts are thus devoted to developing Ni-based nanocatalysts for hydrogenation. Unfortunately, the hydrogenation activity of pure Ni is generally limited under mild conditions due to the inappropriate hydrogen adsorption energies. There is now demand for Ni-based nanocatalysts with high performance.

The crucial step in hydrogenation reactions involves intermediate adsorption and subsequent conversion into product on the nanocatalyst surface [16]. In such a process, charge interaction between adsorbed species and the catalyst surface plays a determining role [17]. Current strategies to tune the intermediate binding on active sites include doping the metal with a second element, introducing

strain effect, or adjusting the exposed facets [18–20]. The central concept of these strategies is to manipulate the local electronic structure of the active sites. No matter which strategy is adopted to tune the electronic structure of the metal nanocatalyst, the nanometals are generally supported on an oxide substrate with a large specific surface area. In this scenario, interactions with the oxide support significantly impact the electronic structures and in turn the catalytic performance of nanometals [21,22]. Recently, we have demonstrated that the electron exchange between the two phases is highly correlated with the Fermi level of the oxide support [23]. The electron density and Fermi level of oxides can be tailored by breaking the symmetry or stoichiometry of the crystal structure, such as defects engineering [24,25] or doping [26,27], resulting in changes in catalytic activity and activation energy of the catalysts. In particular, oxygen vacancies (O_v) of the oxide support enhance the charge donation to the supported metals forming a well-oriented space charge layer [28]. It has been shown that the surface O_v of NiO nanorods significantly enhances the electron conduction and promotes HER (hydrogen evolution reaction) kinetics [29]. However, the intentionally formed excess oxygen vacancies could be progressively annihilated during catalysis at elevated temperatures because the oxide stays at the thermodynamic metastable state and requires a mechanism to maintain the concentration of the O_v. For this purpose, using oxide containing the same element with the supported metal nanoparticles to build the heterostructure would be effective for maintaining the level of oxygen defects in the oxide due to the thermodynamic equilibrium between the two phases.

In this work, we report the fabrication of 2D Ni/NiO nanocomposites with abundant oxygen vacancies (O_v) by in situ growth of Ni on a NiO support. The Al, as the sacrificial agent, is introduced to direct the growth of the $Ni(OH)_2$ nanosheet, which is mainly involved in the formation of a hydrotalcite-like intermediate and subsequent conversion to $Ni(OH)_2$ by hydrothermal treatment. At the same time, much of the Al can be etched out during the hydrothermal process, so that the mesh-like plate can form as a product. The obtained nanocomposites show a large amount of O_v on the surface and the abundant defects are beneficial for the adsorption of 4-NP and hydrogen by the enhanced electronic interaction. Moreover, the total amounts of O_v of the nanocomposites can be tuned by the reduction temperature. The resulting Ni/NiO nanocomposites exhibit excellent catalytic performance for hydrogenating p-nitrophenol to p-aminophenol by $NaBH_4$. The successful synthesis of 2D Ni/NiO nanocomposites with abundant O_v paves the way for the design of highly efficient catalysts.

2. Results and Discussion

2.1. Formation of Ni/NiO Nanocomposites

The fabrication of hexagonal Ni/NiO nanocomposites was achieved via H_2 reduction of hydrothermal-grown $Ni(OH)_2$ nanosheets. Figure 1 shows the XRD profiles of the as-synthesized samples, depicting the transition process of $Ni(OH)_2$ into Ni/NiO. The hydrothermal products were assigned to $Ni(OH)_2$ structure (JCPDS No. 73-1520) and were ready to decompose into NiO (JCPDS No. 75-0197) at the relative low temperature of 250 °C. Due to the release of the H_2O molecular during the decomposition, the crystallinity of the NiO product is low, as expected, which is evidenced by the broad diffraction peaks. Increasing the reduction temperature would produce Ni nanoparticles in the NiO matrix. Metallic Ni appears when the reduction temperature reaches 300 °C and its content increases with a reduction in temperature. The sample heated at 450 °C is mainly composed of metallic Ni and the broadening of diffraction peaks is still obvious, indicating the size of the Ni products is at the nanoscale. Notably, the Al signal peak in XRD disappears due to their low content, although some residuals are observed in the EDS spectrum.

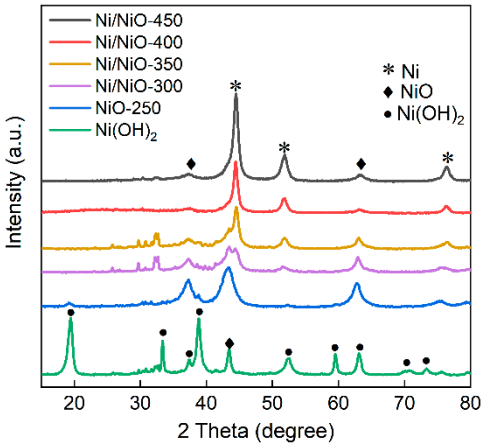

Figure 1. XRD patterns of the $Ni(OH)_2$, NiO-250, Ni/NiO-300, Ni/NiO-350, Ni/NiO-400 and Ni/NiO-450 catalysts compared with the standard pattern of Ni, NiO and $Ni(OH)_2$.

The morphology of the products at different stages was observed by SEM. Figure 2 shows that the hydrothermal grown $Ni(OH)_2$ nanosheets have a hexagonal shape with the length of between 50–90 nm. After thermal decomposition, the NiO inherits the uniform nanosheet structure of the $Ni(OH)_2$ precursor. Ni particles were grown on nanosheets at a reduction temperature of 300 °C, in good agreement with the XRD analysis. Ni/NiO nanocomposites prepared by thermal reduction are expected to have a strong interaction across the interface [30]. Interestingly, the Ni nanoparticles grow preferentially at the edge positions of the nanosheets. We deduce that the Ni–O bonding at the edge position is weaker than that on the plane surface. Two parallel processes exist during the growth of Ni nanoparticles: one is the reduction of NiO to Ni, and the other is the ripening of the reduced Ni. The growth of Ni particles is accomplished by breaking the surface Ni–O bond and the subsequent surface diffusion of the Ni atoms. In thermodynamics, Ni diffusion is driven by the energy difference between the adhesion energy of the Ni atom on the NiO surface and the inherent binding energy of metallic Ni [31]. Therefore, the size and distribution of metallic Ni nanoparticles, as well as the ratio between Ni and NiO, could be tuned by controlling the reduction temperature and the duration. At a higher temperature of 400 °C, a dense distribution of Ni nanoparticles on the nanosheet surface plane is observed, indicating that the kinetic rates of the two processes are comparable. Further increasing the reduction temperature could cause sintering of the nanocomposites (Figure 2f).

The morphology and crystal structures of products at intermediate stages were further confirmed using TEM. Figure 3 demonstrates the Ni/NiO nanocomposite converted from hydrothermal-grown $Ni(OH)_2$ nanosheets by H_2 reduction at 250 °C and 350 °C, showing the inheritance of plate shape. The Fourier transform pattern confirms the hexagonal symmetry in agreement with the [010] axis. Therefore, the exposed facet of the obtained NiO is in the {010} plane. However, the nanosheets obtained at 250 °C are polycrystalline, indicating that the formation of NiO by $Ni(OH)_2$ dehydration nucleates at different sites of the nanosheets. The interplanar spacing of 0.24 nm and 0.27 nm in Figure 3b corresponds to (101) of NiO and (100) of $Ni(OH)_2$, respectively. Brunauer–Emmett–Teller (BET) surface areas and pore size distributions were measured and are summarized in Table S1 and Figure S1. As expected, the surface areas are strikingly enhanced to 40.4 m^2/g in NiO-250. Figure S2 and Figure 3c show that the Ni particles are sufficiently formed from the NiO matrix at 350 °C, resulting in a large number of active sites. The neighboring lattice fringe spacings of 0.2 nm and 0.24 nm correspond to the (200) and (111) planes of NiO, respectively [32]. Another 0.17 nm plane spacing is well matched to the metal Ni $d_{(200)}$ spacing (JCPDS No. 65-2865), indicating that the sample consists of a NiO matrix and embedded metal Ni nanoparticles (Figure 3d).

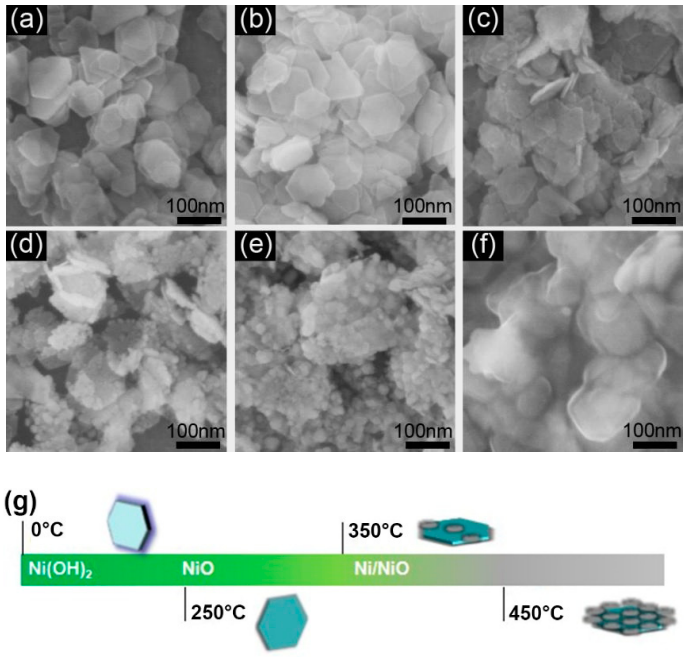

Figure 2. SEM images of the as-prepared products. Hydrothermal grown $Ni(OH)_2$ (**a**); samples after H_2 reduction at 250 °C (**b**), 300 °C (**c**), 350 °C (**d**), 400 °C (**e**), and 450 °C (**f**). (**g**) Schematic illustration of the conversion of samples starting from $Ni(OH)_2$.

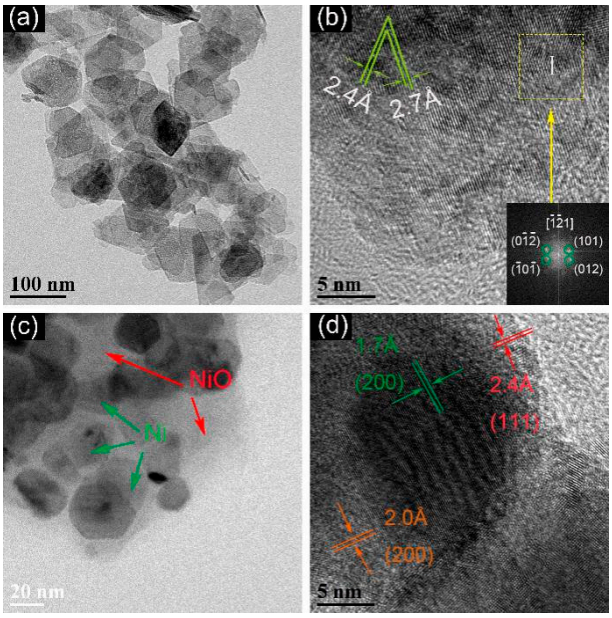

Figure 3. TEM and HRTEM image of the $Ni(OH)_2$ converted products after H_2 reduction at 250 °C (**a**,**b**) and 350 °C (**c**,**d**). Inset: FFT pattern of the rectangle region.

The mixture of metallic Ni and nickel oxide of the as-synthesized samples was confirmed by X-ray photoelectron spectroscopy (XPS). Figure 4 shows the XPS spectra of the as-synthesized Ni/NiO nanocomposites. The two peaks at ~855eV and ~872eV were assigned to the $2p_{3/2}$ and $2p_{1/2}$ of Ni. The two satellite peaks at ~862eV and ~880eV represent the main peak and satellite peak of Ni^{2+} $2p_{1/2}$, respectively, indicating that the existence state of Ni in the two samples is only Ni^{2+}, which exists in the form of $Ni(OH)_2$ or NiO. For Ni/NiO-350, the binding energy values of ~853 eV and ~871 eV were observed, corresponding to Ni^0 $2p_{3/2}$ and $2p_{1/2}$, respectively [33]. This result confirms that the surface of the Ni/NiO-350 sample consists of both Ni^0 and NiO. Under reduction conditions in a H_2

atmosphere, the $Ni(OH)_2$ precursor was reduced to the NiO intermediate in 250 °C, then the generated NiO intermediate was further reduced to Ni at 350 °C, but a thin NiO layer remains due to re-oxidation in air. After reduction at 450 °C, Ni nanoparticles agglomerate to form large Ni particles and the products lose the sheet-like shape.

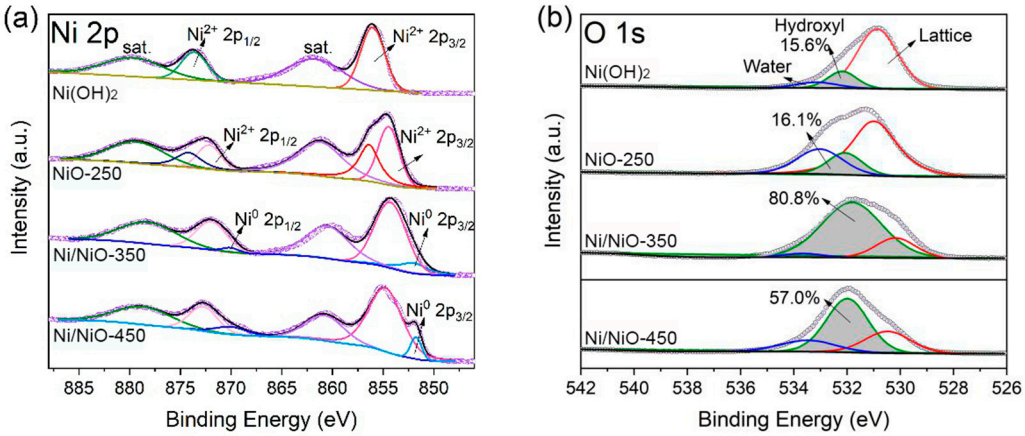

Figure 4. XPS spectra of the (**a**) Ni 2*p* and (**b**) O 1s for all catalysts.

The high-resolution O 1s XPS spectra was deconvoluted into three peaks as shown in Figure 4b. The peaks located at 530.6 eV, 531.9 eV, and 533.3 eV could be attributed to lattice oxygen (Ni–O), adsorbed oxygen and absorbed water on the surfaces of the catalysts, respectively [34,35]. In addition, the peak centered at 531.9 eV is related to a large number of defect sites with lower oxygen coordination [29] and its content in all as-prepared nanocomposites is displayed in Figure 4b. The detailed analysis indicates that the O-vacancies are mainly located on the outermost surface of the Ni/NiO samples (near below 20 nm, Figure S3), which is highly beneficial for fine-tuning the surface chemical and electronic structures, and finally regulating their reactivity [29]. Notably, with a rising reduction temperature, the concentration of O-vacancies in the sample firstly increased and then decreased. The highest concentration in O_v is obtained at NiO prepared at 350 °C. Though higher temperature favors the formation of O-vacancies [36], excessive reduction temperature eliminates the oxide phase and causes sintering of Ni/NiO-450. Therefore, 2D nanocomposites with abundant oxygen defects were successfully prepared in our work. For metal nanoparticles dispersed on an oxide support, the oxygen vacancy in the oxide impacts the electronic interaction across the interface [28,37]. Therefore, many material strategies have been proposed for engineering the oxide defects. However, the oxygen vacancies created by reduction have a strong tendency to be recovered [38]. In this work, the oxygen vacancies in the NiO are expected to be maintained because the NiO has a direct contact with Ni. Therefore, the stability of O_V in NiO is guaranteed by the thermodynamics of the Ni–NiO couple.

2.2. Catalytic Performance

The catalytic activity of the nanosheet Ni/NiO composite was evaluated using hydrogenation of p-nitrophenol by $NaBH_4$. Pure Ni nanocrystals show limited activity for catalyzing the hydrogenation reaction from p-nitrophenol to p-aminophenol [39]. This reaction process could be monitored by scanning the light absorption profile of the solution. In this study, the peak intensity at 400 nm is selected to represent the concentration of p-nitrophenol, while the intensity at 300 nm stands for the concentration of p-aminophenol. As shown in Figure 5a, by adding the Ni/NiO-350 catalyst to the p-nitrophenol solution containing $NaBH_4$, the absorption band at 400 nm gradually weakened, while a new band at 300 nm appeared. Because the light absorption coefficients of AP and NP are different, the variation in absorbance peak does not match. The evolution in light absorption is widely adopted in the literature to reflect the hydrogenation reaction where the p-nitrophenol molecule is directly translated into the p-aminophenol [40,41] Within 5 min, the conversion of p-nitrophenol achieved

100% over the Ni/NiO-350 sample. Figure 5b shows the evolution of nitrophenol concentration over different Ni/NiO nanocatalysts. It was found that the reactivity of nanocomposites follows: NiO-250 < Ni/NiO-300 < Ni/NiO-450 < Ni/NiO-400 < Ni/NiO-350.

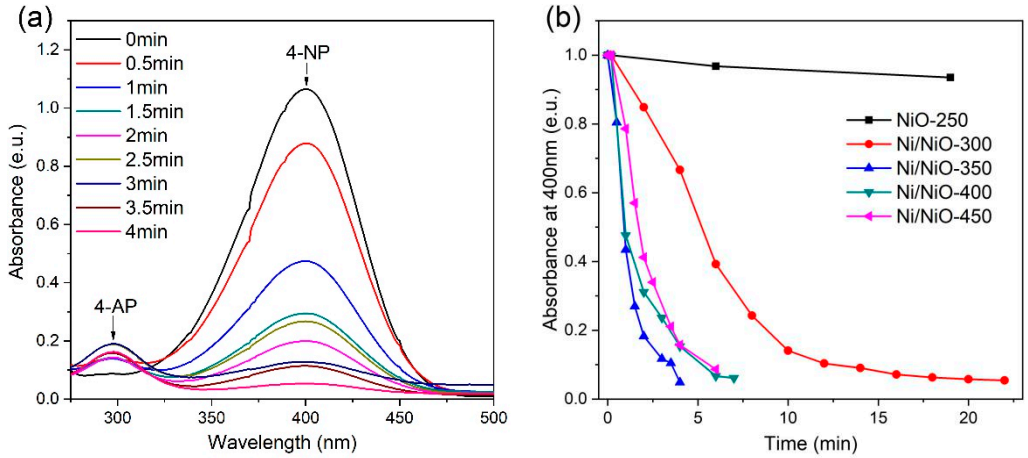

Figure 5. Catalytic performance of the samples for the p-nitrophenol reaction. (**a**) UV−vis spectra of Ni/NiO-350 (the intensity of the band at 400 nm) at various reaction times. (**b**) UV−vis spectra monitored at the band of 400 nm.

For hydrogenation of nitrophenol using $NaBH_4$ as the hydrogen source, the concentration of the borohydride ion was higher than those of p-nitrophenol and Ni/NiO catalysts, so pseudo-first-order kinetics could be applied to investigate the reaction [42]. The pseudo-first-order rate constant k was calculated from the equation $-kt = \ln(C_t/C_0)$, where C_t and C_0 stand for the concentrations of p-nitrophenol at the time of t and at the beginning of the reaction, respectively [42]. The rate constants (k) of all Ni/NiO nanocomposites are listed in Table S2. Ni/NiO-350 shows the highest activity among all samples. The outstanding catalytic performance could be attributed to the dense and uniform distribution of Ni nanoparticles on the oxide, accompanying the high concentration of oxygen vacancies.

2.3. Magnetic Performance

As the metallic Ni is included in the final products, they exhibit room temperature ferromagnetism that facilitates recovery of the catalyst after the catalytic reaction and recycling. Figure 6 depicts the room-temperature magnetic hysteresis loop of the 2D Ni/NiO nanocomposites. The saturation magnetization (M_S) of the Ni/NiO nanocomposites ranges from 6.7 emu g^{-1} to 12.7 emu g^{-1}, and the coercive force (H_c) ranges from 7.5 Oe to 91.7 Oe. The Ni/NiO composite obtained by hydrogen reduction has a large M_S and H_c. For composite materials, M_S is related to the content of the magnetic phase [39]. In this work, the presence of Ni nanoparticles in the Ni/NiO composite microstructure leads to a high M_S.

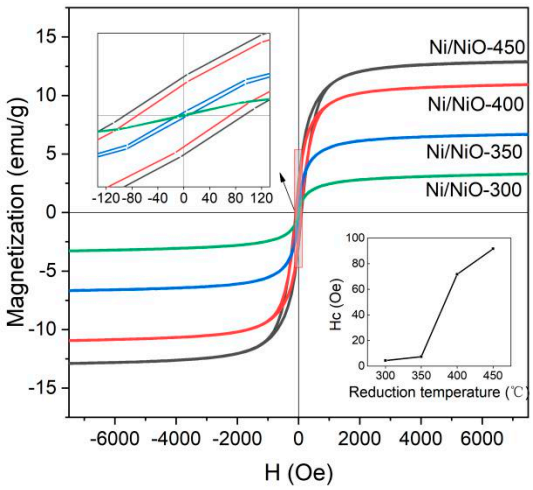

Figure 6. The room-temperature magnetic hysteresis loop of the 2D Ni/NiO nanocomposites.

3. Materials and Methods

3.1. Materials

Nickel nitrate ($Ni(NO_3)_2{\cdot}6H_2O$, AR) and potassium hydroxide (KOH, AR) were purchased from SinoPharm Chemical Reagent Corp (Shenyang, China), and aluminum powder (Al, 99.5%) from Aladdin (Shanghai, China). All chemicals and solvents were used without further purification.

3.2. Synthesis of Samples

$Ni(OH)_2$ precursor: The catalysts were synthesized using a hydrothermal method [43]. In a typical preparation, 1.1632 g $Ni(NO_3)_2{\cdot}6H_2O$ was dissolved in 30 mL of deionized water and the solution was stirred for 30 min. KOH solution (2.5 M, 40 mL) was then added dropwise into the nickel nitrate solution with a speed of ~1 mL/min under vigorous stirring for 1 h. Immediately after 0.2698 g aluminum powder was added, the mixture was sealed in a Teflon-lined steel autoclave and maintained at 200 °C for 20 h. Finally, the obtained precipitates were centrifuged and washed with deionized water before drying at 60 °C overnight under vacuum.

Ni/NiO nanocomposites: The dried precursor was then calcined in a furnace at different calcination temperatures under flowing 10 vol % H_2/He (100 mL min^{-1}) for 2 h. In this study, the reduction temperature ranged between 250 °C and 450 °C. The obtained nanocomposites were named Ni/NiO-T (T represents the reduction temperature). By regulating the reduction temperature, we obtained sample NiO-200, NiO-250, Ni/NiO-300, Ni/NiO-350, Ni/NiO-400, Ni/NiO-450.

3.3. Structural Characterizations

Powder X-ray diffraction (XRD) was used to determine the crystal structure of the samples on a Phillips X-Pert X-ray diffractometer (Almelo, Netherlands) (Cu KR radiation, λ = 1.5418 Å) at 40 kV and 15 mA. The scanning electron microscopy (Tokyo, Japan) (SEM) images were recorded using a Hitachi SU8020 scanning electron microscope. Transmission electron microscopy (TEM) images were taken on Tecnai G2S-TwinF20 equipped with energy dispersive spectroscopy (EDS) (Akishima, Japan). Surface chemical states were analyzed by X-ray photoelectron spectroscopy (XPS, PHI 5000 Versaprobe) with Al-Kα excitation. The charging shift was calibrated using a C 1s photoemission line at 284.8 eV. Raman spectra were collected on an INVIA Raman system under excitation of 532 nm. Nitrogen adsorption–desorption measurements were carried out on an ASAP 2020 instrument (Shah Alam, Selangor, Malaysia). Before the measurement, all the catalyst samples were degassed at 200 °C under vacuum for 2 h. The specific surface areas of samples were determined by N_2 adsorption/desorption

isotherms at 77 K collected on an ASAP 2460 gas adsorption analyzer. Magnetic properties were measured on a vibrating sample magnetometer (VSM) at room temperature.

3.4. Catalytic Activity Measurements

The as-obtained Ni/NiO nanocomposites were used as catalyst for the hydrogenation of 4-nitrophenol using $NaBH_4$ as a hydrogen source. In a typical procedure, 25 mL 4-nitrophenol solution (0.072 mol/L) and 25 mL $NaBH_4$ solution (0.72 mol/L) were mixed in a 100-mL beaker under stirring at 1000 r min^{-1} at room temperature, atmospheric pressure and then 5 mg of catalysts were added into the system to trigger the catalytic reaction. The reaction processes were monitored by UV–vis spectroscopy [44]. During the reaction process, 2 mL of reaction solution was withdrawn every 30 s and then immediately dispersed back after measurement.

4. Conclusions

In summary, we have demonstrated a simple hydrothermal method and subsequent hydrogen reduction for the preparation of uniform 2D Ni/NiO nanocomposites. The nanocomposites were obtained by heating $Ni(OH)_2$ nanosheets in H_2 flow. Balancing the reduction of NiO and the ripening of the resulted Ni nanoparticles plays a critical role in controlling the Ni nanoparticle distribution on the NiO surface. The hexagonal 2D Ni/NiO nanocomposites exhibit excellent catalytic activity for the reduction of 4-nitrophenol to 4-aminophenol in $NaBH_4$ solution. The high hydrogenation activity of the Ni/NiO nanocomposite resulted from the interfacial electronic interaction enhanced by the rich oxygen vacancies in the NiO. In addition, the ferromagnetic feature of the nanocomposites renders them easy to recover and reuse after the reaction.

Supplementary Materials: The following are available online at http://www.mdpi.com/2073-4344/9/11/944/s1, Figure S1: N_2 adsorption–desorption isotherms and pore size distribution, Figure S2: TEM image of the Ni/NiO after reduction at 350 °C, Figure S3: EDS mapping and TEM images of Ni/NiO-350 sample, Table S1: Textural properties of the Ni/NiO nanocomposites.

Author Contributions: Sample preparation and characterization, J.Z. and Y.Z.; discussion, J.C.; writing—original draft preparation, Y.Z.; writing—review and editing, S.L.

Funding: The work was supported by the Fundamental Research Funds for the Central Universities (N180204014, N170204015) and the National Natural Science Foundation of China (51601032, 51601119). J. Chen thanks the Key Lab for ATM of Northeastern University of China and the Natural Science Foundation of Shenzhen University (2019006, 860-000002110422).

Conflicts of Interest: The authors declare no conflict of interest.

References

1. Liu, W.; Jiang, Y.; Dostert, K.H.; O'Brien, C.P.; Riedel, W.; Savara, A.; Schauermann, S.; Tkatchenko, A. Catalysis beyond frontier molecular orbitals: Selectivity in partial hydrogenation of multi-unsaturated hydrocarbons on metal catalysts. *Sci. Adv.* **2017**, *3*, e1700939. [CrossRef] [PubMed]
2. Wang, L.; Guan, E.; Zhang, J.; Yang, J.; Zhu, Y.; Han, Y.; Yang, M.; Cen, C.; Fu, G.; Gates, B.C.; et al. Single-site catalyst promoters accelerate metal-catalyzed nitroarene hydrogenation. *Nat. Commun.* **2018**, *9*, 1362. [CrossRef] [PubMed]
3. Feng, Q.; Zhao, S.; Xu, Q.; Chen, W.; Tian, S.; Wang, Y.; Yan, W.; Luo, J.; Wang, D.; Li, Y. Mesoporous nitrogen-doped carbon-nanosphere-supported isolated single-atom Pd catalyst for highly efficient semihydrogenation of acetylene. *Adv. Mater.* **2019**, *31*, 1901024. [CrossRef] [PubMed]
4. Ai, Y.; Hu, Z.; Liu, L.; Zhou, J.; Long, Y.; Li, J.; Ding, M.; Sun, H.; Liang, Q. Magnetically hollow Pt nanocages with ultrathin walls as a highly integrated nanoreactor for catalytic transfer hydrogenation reaction. *Adv. Sci.* **2019**, *6*, 1802132. [CrossRef]
5. Gu, K.; Pan, X.; Wang, W.; Ma, J.; Sun, Y.; Yang, H.; Shen, H.; Huang, Z.; Liu, H. In Situ Growth of Pd nanosheets on g-C_3N_4 nanosheets with well-contacted interface and enhanced catalytic performance for 4-nitrophenol reduction. *Small* **2018**, *14*, 1801812. [CrossRef]

6. Vilé, G.; Albani, D.; Almora-Barrios, N.; López, N.; Pérez-Ramírez, J. Advances in the design of nanostructured catalysts for selective hydrogenation. *ChemCatChem* **2016**, *8*, 21–33. [CrossRef]
7. Jarrais, B.; Guedes, A.; Freire, C. Heteroatom-doped carbon nanomaterials as metal-free catalysts for the reduction of 4-nitrophenol. *ChemistrySelect* **2018**, *3*, 1737–1748. [CrossRef]
8. Wang, Z.; Su, R.; Wang, D.; Shi, J.; Wang, J.X.; Pu, Y.; Chen, J.F. Sulfurized graphene as efficient metal-free catalysts for reduction of 4-nitrophenol to 4-aminophenol. *Ind. Eng. Chem. Res.* **2017**, *56*, 13610–13617. [CrossRef]
9. Liu, J.; Yan, X.; Wang, L.; Kong, L.; Jian, P. Three-dimensional nitrogen-doped graphene foam as metal-free catalyst for the hydrogenation reduction of p-nitrophenol. *J. Colloid Interface Sci.* **2017**, *497*, 102–107. [CrossRef]
10. Pozun, Z.D.; Rodenbusch, S.E.; Keller, E.; Tran, K.; Tang, W.; Stevenson, K.J.; Henkelman, G. A Systematic investigation of p-nitrophenol reduction by bimetallic dendrimer encapsulated nanoparticles. *J. Phys. Chem. C* **2013**, *117*, 7598–7604. [CrossRef]
11. Gupta, V.K.; Yola, M.L.; Eren, T.; Kartal, F.; Çağlayan, M.O.; Atar, N. Catalytic activity of Fe@Ag nanoparticle involved calcium alginate beads for the reduction of nitrophenols. *J. Mol. Liq.* **2014**, *190*, 133–138. [CrossRef]
12. Chen, Q.; Zhang, P.; Li, R.; Huang, Y. A novel approach for the in situ synthesis of Pt-Pd nanoalloys supported on Fe_3O_4@C core-shell nanoparticles with enhanced catalytic activity for reduction reactions. *ACS Appl. Mater. Interfaces* **2014**, *6*, 2671–2678.
13. Gupta, V.K.; Atar, N.; Yola, M.L.; Üstündağ, Z.; Uzun, L. A novel magnetic Fe@Au core-shell nanoparticles anchored graphene oxide recyclable nanocatalyst for the reduction of nitrophenol compounds. *Water Res.* **2014**, *48*, 210–217. [CrossRef] [PubMed]
14. Saha, S.; Pal, A.; Kundu, S.; Basu, S.; Pal, T. Photochemical green synthesis of calcium-alginate-stabilized ag and au nanoparticles and their catalytic application to 4-nitrophenol reduction. *Langmuir* **2010**, *26*, 2885–2893. [CrossRef] [PubMed]
15. Zhang, P.; Shao, C.; Zhang, Z.; Zhang, M.; Mu, J.; Guo, Z.; Liu, Y. In situ assembly of well-dispersed Ag nanoparticles (AgNPs) on electrospun carbon nanofibers (CNFs) for catalytic reduction of 4-nitrophenol. *Nanoscale* **2011**, *3*, 3357–3363. [CrossRef]
16. Andersen, M.; Medford, A.J.; Nørskov, J.K.; Reuter, K. Scaling-relation-based analysis of bifunctional catalysis: the case for homogeneous bimetallic alloys. *ACS Catal.* **2017**, *7*, 3960–3967. [CrossRef]
17. Abdel-Mageed, A.M.; Klyushin, A.; Rezvani, A.; Knop-Gericke, A.; Schlögl, R.; Behm, R.J. Negative charging of Au nanoparticles during methanol synthesis from CO_2 /H_2 on a Au/ZnO catalyst: Insights from operando IR and near-ambient-pressure XPS and XAS measurements. *Angew. Chemie Int. Ed.* **2019**, *58*, 10325–10329. [CrossRef]
18. Zhu, X.; Guo, Q.; Sun, Y.; Chen, S.; Wang, J.Q.; Wu, M.; Fu, W.; Tang, Y.; Duan, X.; Chen, D.; et al. Optimising surface d charge of AuPd nanoalloy catalysts for enhanced catalytic activity. *Nat. Commun.* **2019**, *10*, 1428. [CrossRef]
19. Yao, Y.; Hu, S.; Chen, W.; Huang, Z.Q.; Wei, W.; Yao, T.; Liu, R.; Zang, K.; Wang, X.; Wu, G.; et al. Engineering the electronic structure of single atom Ru sites via compressive strain boosts acidic water oxidation electrocatalysis. *Nat. Catal.* **2019**, *2*, 304–313. [CrossRef]
20. Xu, C.; Wu, Y.; Li, S.; Zhou, J.; Chen, J.; Jiang, M.; Zhao, H.; Qin, G. Engineering the epitaxial interface of Pt-CeO_2 by surface redox reaction guided nucleation for low temperature CO oxidation. *J. Mater. Sci. Technol.* **2019**. [CrossRef]
21. Lykhach, Y.; Kozlov, S.M.; Skála, T.; Tovt, A.; Stetsovych, V.; Tsud, N.; Dvořák, F.; Johánek, V.; Neitzel, A.; Mysliveček, J.; et al. Counting electrons on supported nanoparticles. *Nat. Mater.* **2016**, *15*, 284–288. [CrossRef] [PubMed]
22. Ghosh, S.; Mammen, N.; Narasimhan, S. Descriptor for the efficacy of aliovalent doping of oxides and its application for the charging of supported Au clusters. *J. Phys. Chem. C* **2019**, *123*, 19794–19805. [CrossRef]
23. Liu, Y.; Chen, H.; Xu, C.; Sun, Y.; Li, S.; Jiang, M.; Qin, G. Control of catalytic activity of nano-Au through tailoring the Fermi level of support. *Small* **2019**, *15*, 1901789. [CrossRef] [PubMed]
24. Cao, F.; Wang, Y.; Wang, J.; Lv, X.; Liu, D.; Ren, J.; Zhou, J.; Deng, R.; Li, S.; Qin, G. Oxygen vacancy induced superior visible-light-driven photodegradation pollutant performance in BiOCl microflowers. *New J. Chem.* **2018**, *42*, 3614–3618. [CrossRef]

25. Tran, S.B.T.; Choi, H.; Oh, S.; Park, J.Y. Defective Nb_2O_5-supported Pt catalysts for CO oxidation: Promoting catalytic activity via oxygen vacancy engineering. *J. Catal.* **2019**, *375*, 124–134. [CrossRef]
26. Mammen, N.; de Gironcoli, S.; Narasimhan, S. Substrate doping: A strategy for enhancing reactivity on gold nanocatalysts by tuning sp bands. *J. Chem. Phys.* **2015**, *143*, 144307. [CrossRef]
27. Li, S.; Cai, J.; Liu, Y.; Gao, M.; Cao, F.; Qin, G. Tuning orientation of doped hematite photoanodes for enhanced photoelectrochemical water oxidation. *Sol. Energy Mater. Sol. Cells* **2018**, *179*, 328–333. [CrossRef]
28. Schneider, W.D.; Heyde, M.; Freund, H.J. Charge control in model catalysis: the decisive role of the oxide–nanoparticle interface. *Chem. A Eur. J.* **2018**, *24*, 2317–2327. [CrossRef]
29. Zhang, T.; Wu, M.Y.; Yan, D.Y.; Mao, J.; Liu, H.; Hu, W.B.; Du, X.W.; Ling, T.; Qiao, S.Z. Engineering oxygen vacancy on NiO nanorod arrays for alkaline hydrogen evolution. *Nano Energy* **2018**, *43*, 103–109. [CrossRef]
30. Wang, Y.; Cao, F.; Lin, W.; Zhao, F.; Zhou, J.; Li, S.; Qin, G. In situ synthesis of Ni/NiO composites with defect-rich ultrathin nanosheets for highly efficient biomass-derivative selective hydrogenation. *J. Mater. Chem. A* **2019**, *7*, 17834–17841. [CrossRef]
31. Zeng, Y.; Meng, Y.; Lai, Z.; Zhang, X.; Yu, M.; Fang, P.; Wu, M.; Tong, Y.; Lu, X. An Ultrastable and High-Performance Flexible Fiber-Shaped Ni-Zn Battery based on a Ni-NiO Heterostructured Nanosheet Cathode. *Adv. Mater.* **2017**, *29*, 1702698. [CrossRef] [PubMed]
32. Ma, Q.; Sun, J.; Gao, X.; Zhang, J.; Zhao, T.; Yoneyama, Y.; Tsubaki, N. Ordered mesoporous alumina-supported bimetallic Pd-Ni catalysts for methane dry reforming reaction. *Catal. Sci. Technol.* **2016**, *6*, 6542–6550. [CrossRef]
33. Liu, Y.; Zhao, J.; Feng, J.; He, Y.; Du, Y.; Li, D. Layered double hydroxide-derived Ni-Cu nanoalloy catalysts for semi-hydrogenation of alkynes: Improvement of selectivity and anti-coking ability via alloying of Ni and Cu. *J. Catal.* **2018**, *359*, 251–260. [CrossRef]
34. Li, H.; Li, L.; Fang, S.; Wang, J.; Chen, S.; Huang, X.; Leng, Z.; Li, G. Surface hydroxylation induced by alkaline-earth metal doping in NiO nanocrystals and its application in achieving a wide temperature operation window for preferential CO oxidation. *Environ. Sci. Nano* **2018**, *5*, 2368–2381. [CrossRef]
35. Xu, C.; Li, S.; Zhang, Y.; Li, Y.; Zhou, J.; Qin, G. Synthesis of CuO_x-CeO_2 catalyst with high-density interfaces for selective oxidation of CO in H_2-rich stream. *Int. J. Hydrogen Energy* **2019**, *44*, 4156–4166. [CrossRef]
36. Cheng, F.; Zhang, T.; Zhang, Y.; Du, J.; Han, X.; Chen, J. Enhancing electrocatalytic oxygen reduction on MnO_2 with vacancies. *Angew. Chemie Int. Ed.* **2013**, *52*, 2474–2477. [CrossRef] [PubMed]
37. Pacchioni, G.; Freund, H.J. Controlling the charge state of supported nanoparticles in catalysis: Lessons from model systems. *Chem. Soc. Rev.* **2018**, *47*, 8474–8502. [CrossRef]
38. Wang, Y.; Widmann, D.; Heenemann, M.; Diemant, T.; Biskupek, J.; Schlögl, R.; Behm, R.J. The role of electronic metal-support interactions and its temperature dependence: CO adsorption and CO oxidation on Au/TiO_2 catalysts in the presence of TiO_2 bulk defects. *J. Catal.* **2017**, *354*, 46–60. [CrossRef]
39. Yuan, F.; Ni, Y.; Zhang, L.; Yuan, S.; Wei, J. Synthesis, properties and applications of flowerlike Ni-NiO composite microstructures. *J. Mater. Chem. A* **2013**, *1*, 8438–8444. [CrossRef]
40. Deraedt, C.; Salmon, L.; Gatard, S.; Ciganda, R.; Hernandez, R.; Ruiz, J.; Astruc, D. Sodium borohydride stabilizes very active gold nanoparticle catalysts. *Chem. Commun.* **2014**, *50*, 14194–14196. [CrossRef]
41. Zheng, G.; Polavarapu, L.; Liz-Marzán, L.M.; Pastoriza-Santos, I.; Pérez-Juste, J. Gold nanoparticle-loaded filter paper: A recyclable dip-catalyst for real-time reaction monitoring by surface enhanced Raman scattering. *Chem. Commun.* **2015**, *51*, 4572–4575. [CrossRef] [PubMed]
42. Pacardo, D.B.; Ardman, E.; Knecht, M.R. Effects of substrate molecular structure on the catalytic activity of peptide-templated Pd nanomaterials. *J. Phys. Chem. C* **2014**, *118*, 2518–2527. [CrossRef]
43. Ding, J.; Li, L.; Zheng, H.; Zuo, Y.; Wang, X.; Li, H.; Chen, S.; Zhang, D.; Xu, X.; Li, G. Co_3O_4–$CuCoO_2$ nanomesh: An interface-enhanced substrate that simultaneously promotes CO adsorption and O_2 activation in H_2 purification. *ACS Appl. Mater. Interfaces* **2019**, *11*, 6042–6053. [CrossRef] [PubMed]
44. Qin, G.W.; Pei, W.; Ma, X.; Xu, X.; Ren, Y.; Sun, W.; Zuo, L. Enhanced catalytic activity of Pt nanomaterials: From monodisperse nanoparticles to self-organized nanoparticle-linked nanowires. *J. Phys. Chem. C* **2010**, *114*, 6909–6913. [CrossRef]